Spherical topological insulator nanoparticles: Quantum size effects and optical transitions

L. Gioia,[1,2] M. G. Christie,[3] U. Zülicke ●,[3,4,*] M. Governale,[3] and A. J. Sneyd[3]

[1]*Perimeter Institute, 31 Caroline Street North, Waterloo, Ontario, Canada N2L 2Y5*
[2]*Department of Physics and Astronomy, University of Waterloo, Waterloo, Ontario, Canada N2L 3G1*
[3]*School of Chemical and Physical Sciences and MacDiarmid Institute for Advanced Materials and Nanotechnology,*
Victoria University of Wellington, P.O. Box 600, Wellington 6140, New Zealand
[4]*Department of Physics, University of Basel, Klingelbergstrasse 82, CH-4056 Basel, Switzerland*

We have investigated the interplay between band inversion and size quantization in spherically shaped nanoparticles made from topological-insulator (TI) materials. A general theoretical framework is developed based on a versatile continuum-model description of the TI bulk band structure and the assumption of a hard-wall mass confinement. Analytical results are obtained for the wave functions of single-electron energy eigenstates and the matrix elements for optical transitions between them. As expected from spherical symmetry, quantized levels in TI nanoparticles can be labeled by quantum numbers j and $m = -j, -j + 1, \ldots, j$ for total angular momentum and its projection on an arbitrary axis. The fact that TIs are narrow-gap materials, where the charge-carrier dynamics is described by a type of two-flavor Dirac model, requires j to assume half-integer values and also causes a doubling of energy-level degeneracy where two different classes of states are distinguished by being parity eigenstates with eigenvalues $(-1)^{j \mp 1/2}$. The existence of energy eigenstates having the same j but opposite parity enables optical transitions where j is conserved, in addition to those adhering to the familiar selection rule where j changes by ± 1. All optical transitions satisfy the usual selection rule $\Delta m = 0, \pm 1$. We treat intra- and interband optical transitions on the same footing and establish ways for observing unusual quantum-size effects in TI nanoparticles, including oscillatory dependencies of the band gap and of transition amplitudes on the nanoparticle radius. Our theory also provides a unified perspective on multiband models for charge carriers in semiconductors and Dirac fermions from elementary-particle physics.

I. INTRODUCTION AND SYNOPSIS OF MAIN RESULTS

Synthesis and experimental investigation of semiconductor nanocrystals have been pursued with great effort to elucidate how electronic and optical properties of such low-dimensional systems are affected by size-quantization effects [1,2]. Recent advances in the fabrication of nanoparticles made from topological-insulator (TI) materials [3–9] have created the opportunity to explore the interplay of topological properties and quantum confinement [10]. In particular, TI materials are known to host surface states that are robust to perturbations and have energies within the bulk band gap [11–13]. The presence of these surface states is envisioned to enable intriguing applications for TI-based optoelectronics [14], spintronics [15,16], and thermoelectrics [17]. As device fabrication often involves nanostructuring of the TI material, it is necessary to understand the evolution of surface-state properties as the TI nanomaterial's size is reduced [18–23]. Our theoretical description for the electronic and optical properties of spherical TI nanoparticles sheds light on the importance and implications of quantum-size effects in these, and related, nanostructures.

Previous theoretical studies of TI nanoparticles have used atomistic electronic-structure calculations [24], approximate descriptions for the surface states [25,26], discretized versions of effective $\mathbf{k} \cdot \mathbf{p}$ models [25,27–29], and numerical exact diagonalization [30,31] to discuss excitonic properties [24], effects of interactions [30], and disorder [28,31], as well as the emergence of unusual electromagnetic properties [27,29]. Related works have considered idealized Dirac models in curved spaces [32–34] or subject to spherically symmetric quantum confinement [35,36]. Here we obtain the exact spectrum of quantized energies and associated quantum states for nanoparticle confinement of charge carriers described by a spherically symmetric version of the low-energy continuum-model Hamiltonian for bulk TIs [37–39],

$$
H = \left(\frac{\Delta_0}{2} + \frac{\gamma}{k_\Delta} \mathbf{k}^2 \right) \tau_z \otimes \sigma_0 + \gamma (k_z \tau_x \otimes \sigma_z + k_- \tau_x \otimes \sigma_+ + k_+ \tau_x \otimes \sigma_-), \quad (1)
$$

comprising both pseudospin (τ) and real-spin (σ) degrees of freedom [40]. In Eq. (1), $\mathbf{k} \equiv (k_x, k_y, k_z) = -i\nabla$ is the operator for the single-electron wave vector and $k_\pm = k_x \pm i k_y$. Further details of the formalism are discussed in Sec. II, and Table I provides the parameter values applicable to a number of currently available TI materials. We use the remainder of this section to present a selection of key results.

The nanoparticle confinement leads to the emergence of quantized energies $E_j^{(n)}$ for single-electron states labeled by the half-integer total-angular-momentum quantum number

*uli.zuelicke@vuw.ac.nz

TABLE I. Values adopted for parameters in the spherically symmetric effective bulk continuum-model Hamiltonian Eq. (1) to represent currently available topological-insulator materials. The Compton length $R_0 \equiv 2\gamma/|\Delta_0|$ for bulk charge carriers is indicative of the magnitude of the nanoparticle radius R below which the band structure becomes topologically trivial.

	γ (eVÅ)	Δ_0 (eV)	k_Δ (Å^{-1})	R_0 (nm)
Bi_2Te_3[a]	2.4	-0.592	0.026	0.81
Sb_2Te_3[a]	2.4	-0.364	0.066	1.3
Bi_2Se_3[a]	2.2	-0.338	0.13	1.3
HgTe[b]	8.4	-0.303	0.09	5.5
$Pb_{0.81}Sn_{0.19}Se$[c]	3.2	-0.025	0.20	26
$Pb_{0.54}Sn_{0.46}Te$[d]	4.8	-0.030	$\gtrsim 0.25$	32

[a]Reference [41] (parameters averaged over spatial anisotropies).
[b]References [42,43].
[c]Reference [44].
[d]Reference [45].

j and a radial quantum number n. For large-enough nanoparticle radius R, the lowest positive-energy levels $E_j^{(1)}$ are below the bulk conduction-band edge $\Delta_0/2$. These remnants of the topologically protected surface states of the bulk system are pushed to higher energies as R is reduced and, one-by-one starting from the largest j, disappear from the subgap energy range. This is illustrated for the three lowest positive-energy levels in Fig. 1, where we adopted the TI-material Compton length $R_0 \equiv 2\gamma/|\Delta_0|$ and the size-quantization energy scale $E_R \equiv \gamma/R$ as natural units. The values for $\Delta_0/(\gamma k_\Delta)$ used in the calculation of results shown in Figs. 1(a)–1(c) are derived from band-structure parameters given in Table I for Bi_2Se_3, Bi_2Te_3, and Sb_2Te_3, respectively. Clear deviations from the previously determined [25,36] asymptotic large-R behavior $E_j^{(1)} \sim (j + \frac{1}{2})E_R$ occur over a wider range of R/R_0 for larger j and increasing $|\Delta_0|/(\gamma k_\Delta)$. Bi_2Te_3 represents a case with strong deviations in the form of large oscillations and a steep rise in bound-state energy at the smallest values of R/R_0. The Bi_2Te_3 nanoparticle also exhibits gaplessness at two values of R/R_0, and there is a finite range of radii where the $j = 3/2$ level is the lowest-energy state and thus defines the TI-nanoparticle band gap. Similar subband inversions occur

between higher-j levels. The lowest energy level is pushed above the bulk-conduction-band edge for $R < R_c = 2.0 R_0$ ($2.6 R_0$, $5.0 R_0$) in the system representing a Bi_2Se_3 (Sb_2Te_3, Bi_2Te_3) nanoparticle, marking the transition to a nontopological band structure. Thus, although R_0 sets the overall scale for the critical radius below which the TI-nanoparticle spectrum becomes ordinary, the actual value of R_c is typically several times larger.

The wave functions in position (**r**) space for TI-nanoparticle-confined electrons can be written in the universal form

$$\Psi_{jm+}^{(n)}(\mathbf{r}) = \frac{C_{j+}^{(n)}}{2} \begin{pmatrix} \sqrt{\frac{j+m}{j}}\, Y_{j-\frac{1}{2}}^{m-\frac{1}{2}}(\theta,\varphi)\, \phi_{j+\uparrow}^{(n)}(r) \\ \sqrt{\frac{j+1-m}{j+1}}\, Y_{j+\frac{1}{2}}^{m-\frac{1}{2}}(\theta,\varphi)\, \phi_{j-\uparrow}^{(n)}(r) \\ \sqrt{\frac{j-m}{j}}\, Y_{j-\frac{1}{2}}^{m+\frac{1}{2}}(\theta,\varphi)\, \phi_{j+\uparrow}^{(n)}(r) \\ -\sqrt{\frac{j+1+m}{j+1}}\, Y_{j+\frac{1}{2}}^{m+\frac{1}{2}}(\theta,\varphi)\, \phi_{j-\uparrow}^{(n)}(r) \end{pmatrix}, \quad (2a)$$

$$\Psi_{jm-}^{(n)}(\mathbf{r}) = \frac{C_{j-}^{(n)}}{2} \begin{pmatrix} \sqrt{\frac{j+1-m}{j+1}}\, Y_{j+\frac{1}{2}}^{m-\frac{1}{2}}(\theta,\varphi)\, \phi_{j+\uparrow}^{(n)}(r) \\ \sqrt{\frac{j+m}{j}}\, Y_{j-\frac{1}{2}}^{m-\frac{1}{2}}(\theta,\varphi)\, \phi_{j-\uparrow}^{(n)}(r) \\ -\sqrt{\frac{j+1+m}{j+1}}\, Y_{j+\frac{1}{2}}^{m+\frac{1}{2}}(\theta,\varphi)\, \phi_{j+\uparrow}^{(n)}(r) \\ \sqrt{\frac{j-m}{j}}\, Y_{j-\frac{1}{2}}^{m+\frac{1}{2}}(\theta,\varphi)\, \phi_{j-\uparrow}^{(n)}(r) \end{pmatrix} \quad (2b)$$

associated with the ordered set of basis states [37–39]:

$$|P1_-^+, 1/2\rangle \equiv |+\uparrow\rangle, \quad -i|P2_+^-, 1/2\rangle \equiv |-\uparrow\rangle,$$
$$|P1_-^+, -1/2\rangle \equiv |+\downarrow\rangle, \quad i|P2_z^-, -1/2\rangle \equiv |-\downarrow\rangle. \quad (3)$$

Here $Y_{j\pm\frac{1}{2}}^{m\pm\frac{1}{2}}(\theta,\varphi)$ are the familiar spherical harmonics as defined in Ref. [46]. The physically unimportant phase factors $C_{j\kappa}^{(n)}$ are given below [see Eq. (20)]; they were chosen to make contact with mathematical formalisms used to describe massless Dirac fermions confined to move on the surface of the unit sphere [32]. The functions $\phi_{j\tau\sigma}^{(n)}(r)$ are determined by solving a radial Schrödinger equation as explained in greater detail in Sec. II. Noting that the spherical harmonics $Y_{|\lambda|}^\mu$ acquire a factor $(-1)^{|\lambda|}$ under the parity transformation [46], and that the basis states $|+\sigma\rangle$ ($|-\sigma\rangle$) are even (odd)
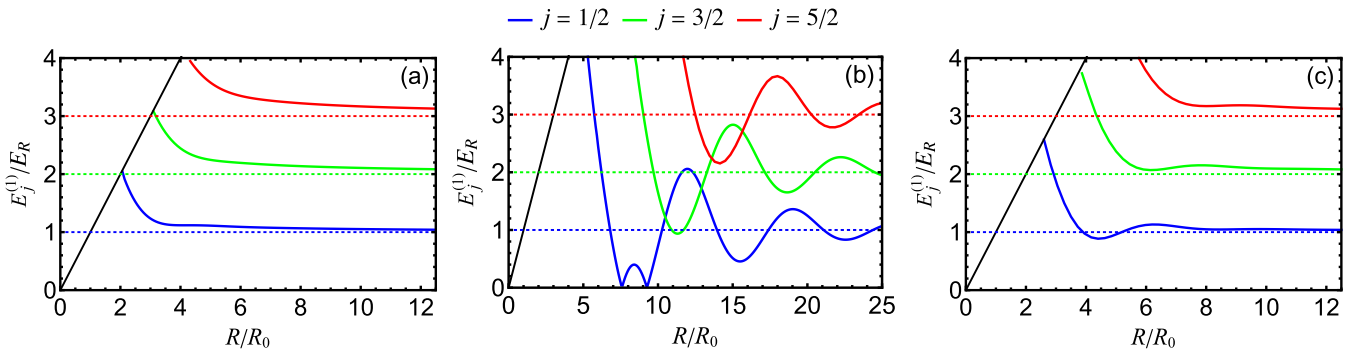

FIG. 1. Energies $E_j^{(1)}$ of quantized electron levels created from topologically protected surface states by a spherical hard-wall mass-confinement potential with radius R. The solid blue (green, red) curve in each panel corresponds to the state with total-angular-momentum quantum number $j = 1/2$ ($j = 3/2$, $j = 5/2$). Here $E_R = \gamma/R$ is the size-quantisation energy scale and $R_0 = 2\gamma/|\Delta_0|$ the bulk Compton length. Results shown in panels (a), (b), and (c) were obtained for fixed $\Delta_0/(\gamma k_\Delta) = -1.2$, -9.5, and -2.3, respectively, which are values representative of Bi_2Se_3, Bi_2Te_3, and Sb_2Te_3 (see Table I for these materials' band-structure parameters). The thin black line indicates the bulk-material conduction-band edge.

under parity [37–39], the wave functions $\Psi_{jm\pm}^{(n)}(\mathbf{r})$ are found to be parity eigenstates with eigenvalue $(-1)^{j\mp\frac{1}{2}}$. The angular part of the wave functions from Eqs. (2) has a structure analogous to that exhibited by localized states in narrow-gap semiconductors [47,48] and spherically symmetric solutions of the Dirac equation [49].

The explicit form of the wave functions in Eqs. (2) enables straightforward calculation of the amplitude for optical transitions between quantized electron states in a TI nanoparticle. In Sec. III, we derive the general expression

$$\mathbf{d} = e\,\mathbf{r}\,\tau_0 \otimes \sigma_0 + \frac{e\,R_0}{2}\,\tau_y \otimes \boldsymbol{\sigma} \qquad (4)$$

for the optical-dipole operator acting in four-dimensional envelope-function space of combined pseudospin (τ) and real-spin (σ) degrees of freedom [40] describing electrons in the TI material [50]. The optical matrix elements

$$\mathbf{d}_{n\,j\,m\kappa}^{n'j'm'\kappa'} \equiv \int d^3r \left[\Psi_{j'm'\kappa'}^{(n')}(\mathbf{r})\right]^\dagger \mathbf{d}\ \Psi_{jm\kappa}^{(n)}(\mathbf{r})\,, \qquad (5)$$

for the transition from an initial state $\Psi_{jm\kappa}^{(n)}$ to a final state $\Psi_{j'm'\kappa'}^{(n')}$ are explicitly found as

$$
\begin{aligned}
(d_x \pm id_y)_{n\,j\,m\kappa}^{n'j'm'\kappa'} = e\,\delta_{m',m\pm1}\Bigg\{&\delta_{\kappa',\kappa}\sum_{\xi=\pm1}\frac{\sqrt{\left[j+\frac{1}{2}+\xi\left(\frac{1}{2}\pm m\right)\right]\left[j+\frac{1}{2}+\xi\left(\frac{3}{2}\pm m\right)\right]}}{2j+1+\xi}\left(\mp\xi\,\mathcal{R}_{n\,j}^{n'j'} \pm i\kappa\,\frac{R_0}{2}\,\mathcal{S}_{n\,j,-\kappa\xi}^{n'j',\kappa\xi}\right)\delta_{j',j+\xi}\\
&+\delta_{\kappa',-\kappa}\frac{\sqrt{(j\mp m)(j+1\pm m)}}{2j(j+1)}\left(\mathcal{R}_{n\,j}^{n'j'}+i\kappa\,\frac{R_0}{2}\left[j\,\mathcal{S}_{n\,j,-\kappa}^{n'j',\kappa}+(j+1)\,\mathcal{S}_{n\,j,\kappa}^{n'j',-\kappa}\right]\right)\delta_{j',j}\Bigg\}\left[C_{j'\kappa'}^{(n')}\right]^*C_{j\kappa}^{(n)}\,, \quad (6a)
\end{aligned}
$$

$$
\begin{aligned}
(d_z)_{n\,j\,m\kappa}^{n'j'm'\kappa'} = e\,\delta_{m',m}\Bigg\{&\delta_{\kappa',\kappa}\sum_{\xi=\pm1}\frac{\sqrt{\left[j+(1+\xi)\frac{1}{2}+m\right]\left[j+(1+\xi)\frac{1}{2}-m\right]}}{2j+1+\xi}\left(\mathcal{R}_{n\,j}^{n'j'}-i\kappa\xi\,\frac{R_0}{2}\,\mathcal{S}_{n\,j,-\kappa\xi}^{n'j',\kappa\xi}\right)\delta_{j',j+\xi}\\
&+\delta_{\kappa',-\kappa}\frac{m}{2j(j+1)}\left[\mathcal{R}_{n\,j}^{n'j'}+i\kappa\,\frac{R_0}{2}\left(j\,\mathcal{S}_{n\,j,-\kappa}^{n'j',\kappa}+(j+1)\,\mathcal{S}_{n\,j,\kappa}^{n'j',-\kappa}\right)\right]\delta_{j',j}\Bigg\}\left[C_{j'\kappa'}^{(n')}\right]^*C_{j\kappa}^{(n)}\,. \quad (6b)
\end{aligned}
$$

For convenience, we have introduced the abbreviation

$$
\begin{aligned}
\mathcal{R}_{n\,j}^{n'j'} = \frac{1}{2}\int_0^\infty dr\ r^3\Big\{&\left[\phi_{j'+\uparrow}^{(n')}(r)\right]^*\phi_{j+\uparrow}^{(n)}(r)+\left[\phi_{j'-\uparrow}^{(n')}(r)\right]^*\\
&\times\phi_{j-\uparrow}^{(n)}(r)\Big\}
\end{aligned}
\qquad (7)
$$

for the matrix element of the radial coordinate between initial and final radial spinor wave functions from Eqs. (2), and the symbols

$$\mathcal{S}_{n\,j,\tau}^{n'j',\tau'} = \int_0^\infty dr\ r^2\left[\phi_{j'\tau'\uparrow}^{(n')}(r)\right]^*\phi_{j\tau\uparrow}^{(n)}(r) \qquad (8)$$

are overlap integrals of radial-wave-function components.

The dependence of matrix elements given in Eqs. (6) on the angular-momentum quantum numbers of the initial and final states embodies selection rules for optical transitions between energy levels in TI nanoparticles. For states with same-type parity ($\kappa' = \kappa$), the rules $j' - j = \pm1$ and $m' - m = 0, \pm1$ are identical to those governing atomic transitions [51]. However, there is also a previously overlooked [36] possibility for transitions between states that are of opposite type with respect to parity (i.e., $\kappa' = -\kappa$), and these follow the unconventional rule $j' - j = 0$ while still adhering to $m' - m = 0, \pm1$. As it turns out, this unconventional type of transition actually determines the low-energy threshold for optical absorption and emission in undoped TI nanoparticles.

The effect of the radial confinement on dipole-allowed single-electron transitions in TI nanoparticles is contained in the matrix elements $\mathcal{R}_{n\,j}^{n'j'}$ and the overlap integrals $\mathcal{S}_{n\,j,\tau}^{n'j',\tau'}$ defined in Eqs. (7) and (8), respectively. In the large-size limit $R \gg R_0$, we find $|\mathcal{R}_{n\,j}^{n'j'}| \sim R$ and $|\mathcal{S}_{n\,j,\mp}^{n'j',\pm}| \sim 1$, reflecting the surface-localized massless-Dirac-fermion character of

low-energy states in this regime. However, as illustrated in Figs. 2(a) and 2(b), significant deviations from this expected limiting behavior occur in the range of small-to-medium nanoparticle sizes $R \gtrsim R_0$. These deviations become more sizable, and also occur over a greater size range, for larger values of the TI-material parameter $-\Delta_0/(\gamma k_\Delta)$.

The remainder of this paper is structured as follows. In Sec. II, the continuum-model description of 3D TIs based on the Hamiltonian from Eq. (1) is used to obtain the spectrum of quantized energies and associated quantum states for a spherical hard-wall mass-confinement potential. Here we derive the general form of the confined-electron eigenspinors given in Eqs. (2) and also find the radial wave functions $\phi_{j\tau\sigma}^{(n)}(r)$. The formalism for describing optical properties of TI nanoparticles is developed in Sec. III. Transitions can be mediated by both the envelope-function part of electron wave functions and also by the Bloch-function basis states. We treat these contributions on the same footing and find a compact expression for a total optical-dipole operator that subsumes both of them [Eq. (4)]. Applying the result from Secs. II and III, we obtain the optical-transition matrix elements given in Eqs. (6). These form the basis for discussing quantum-size effects in TI nanoparticles, focusing especially on their ramifications for optical spectroscopy. Our conclusions are presented in Sec. IV.

II. ELECTRON STATES IN SPHERICALLY SYMMETRIC TI NANOSTRUCTURES

Our starting point is the effective continuum-model Hamiltonian from Eq. (1), which is associated with the set of basis
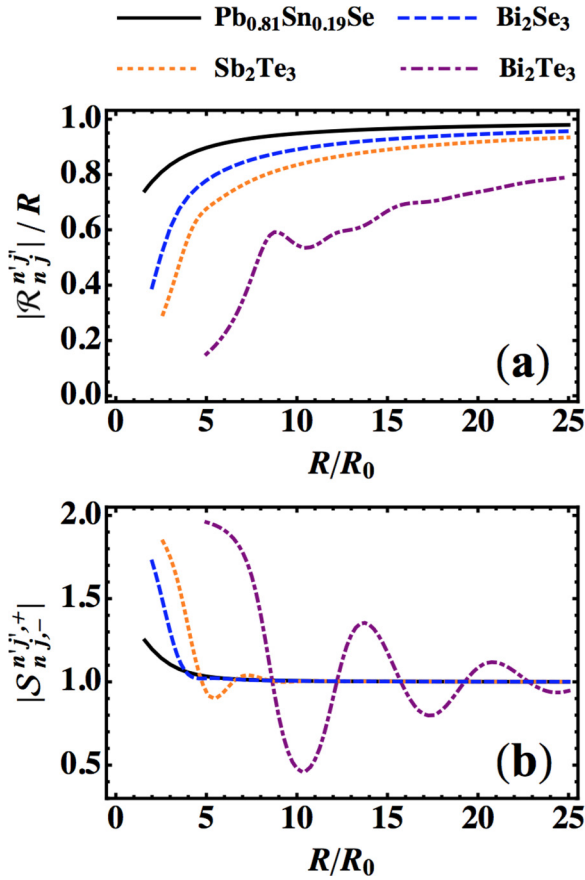
FIG. 2. Dependence of optical-transition amplitudes on TI-nanoparticle size. Panel (a) [(b)] shows the magnitude of the radial-coordinate matrix element $\mathcal{R}^{n'j'}_{nj}$ [the overlap integral $\mathcal{S}^{n'j',+}_{nj,-}$] for $j = j' = 1/2$ and $n = -1$, $n' = 1$, which typically corresponds to the transition across the intrinsic nanoparticle band gap, as a function of the nanoparticle radius R over the range where the lowest confined electron level is still below the bulk-band-gap edge. Here $R_0 = 2\gamma/|\Delta_0|$ is the bulk Compton length, and the black solid (blue dashed, orange dotted, purple dot-dashed) curve corresponds to $\Delta_0/(\gamma k_\Delta) = -0.039\,(-1.2, -2.3, -9.5,)$, which is the value representative of $Pb_{0.81}Sn_{0.19}Se$ (Bi_2Se_3, Sb_2Te_3, Bi_2Te_3). From results presented in panel (b), $|\mathcal{S}^{n'j',-}_{nj,+}| \equiv 2 - |\mathcal{S}^{n'j',+}_{nj,-}|$ can be inferred.

states given in Eq. (3). Throughout this paper, we label basis states $|\tau\,\sigma\rangle$ in terms of pseudospin $\tau \in \{+, -\}$ and real spin $\sigma \in \{\uparrow, \downarrow\}$ [52]. The parameter γ characterizes the interband coupling, and Δ_0 is the energy gap of the bulk-TI material. The term involving k_Δ quantifies remote-band contributions that also provide a natural regularization of the leading Dirac-fermion-like dispersion that is essential for keeping the theory well-defined in the ultrarelativistic limit $\Delta_0 \to 0$. To facilitate an instructive analytical treatment, the often quite sizable deviations from spherical symmetry and particle-hole symmetry in the TI-material bulk dispersions are omitted from the Hamiltonian in Eq. (1), and materials parameters given in Table I correspond to spatial averages.

We first consider the general spherical-confinement problem in Sec. II A. Using a wave-function *Ansatz* involving the known eigenstates of a massless Dirac fermion moving on the surface of the unit sphere [32], we obtain a one-dimensional

radial Schrödinger equation. The latter's solution for a hard-wall mass-confinement potential is presented in Sec. II B.

A. Separation *Ansatz* and radial Schrödinger equation

We envision the TI nanoparticle to be defined by a spherically symmetric mass-confinement potential:

$$H_V = V(r)\,\tau_z \otimes \sigma_0. \tag{9}$$

Then the electronic-bound-state Schrödinger equation $[H + H_V]\Psi = E\,\Psi$ is most conveniently solved by decoupling angular and radial motions. Expressing H in terms of the usual spherical coordinates $\mathbf{r} \equiv (r, \theta, \varphi)$ and using the transformation [25]

$$\mathcal{U}(\theta, \varphi) = \tau_0 \otimes \exp\left(-i\,\frac{\varphi}{2}\,\sigma_z\right)\exp\left(-i\,\frac{\theta}{2}\,\sigma_y\right), \tag{10}$$

it is straightforward to obtain

$$H = \mathcal{U}(\theta, \varphi)(\mathcal{H}^\perp + \mathcal{H}^\parallel)\mathcal{U}^\dagger(\theta, \varphi), \tag{11}$$

with Hamiltonians associated with radial and angular motion, respectively, given by

$$\mathcal{H}^\perp = \left[\frac{\Delta_0}{2} - \frac{\gamma}{k_\Delta}\frac{1}{r^2}\partial_r(r^2\,\partial_r)\right]\tau_z \otimes \sigma_0 - i\,\gamma\left(\partial_r + \frac{1}{r}\right)\tau_x \otimes \sigma_z, \tag{12a}$$

$$\mathcal{H}^\parallel = \frac{\gamma}{r}\left[D\,\tau_x \otimes \sigma_+ + D^\dagger\,\tau_x \otimes \sigma_- + \frac{1}{k_\Delta r}\left(DD^\dagger\,\tau_z \otimes \pi_+\right.\right.$$
$$\left.\left. + D^\dagger D\,\tau_z \otimes \pi_- + i\,D\,\tau_z \otimes \sigma_+ - i\,D^\dagger\,\tau_z \otimes \sigma_-\right)\right]. \tag{12b}$$

Here $\pi_\pm = (\sigma_0 \pm i\sigma_z)/2$ are projection operators on the eigenstates of σ_z in real-spin space, and the operators

$$D = -i\left(\partial_\theta + \frac{\cot\theta}{2} - \frac{i\,\partial_\varphi}{\sin\theta}\right), \tag{13a}$$

$$D^\dagger = -i\left(\partial_\theta + \frac{\cot\theta}{2} + \frac{i\,\partial_\varphi}{\sin\theta}\right) \tag{13b}$$

appear in the Dirac operator on the unit sphere [32].

The spherical mass-confinement potential H_V trivially commutes with the transformation $\mathcal{U}(\theta, \varphi)$, i.e., $\mathcal{H}_V \equiv \mathcal{U}^\dagger(\theta, \varphi)\,H_V\,\mathcal{U}(\theta, \varphi) = H_V$. This feature, together with the structure of the angular-motion Hamiltonian $\mathcal{H}^\parallel$, motivates the separation *Ansatz*

$$\Psi(r, \theta, \varphi) = \mathcal{U}(\theta, \varphi)\frac{e^{im\varphi}}{\sqrt{4\pi}}\begin{pmatrix}\alpha_{\lambda m}(\theta) & \phi_{|\lambda|+\uparrow}(r) \\ \alpha_{\lambda m}(\theta) & \phi_{|\lambda|-\uparrow}(r) \\ \beta_{\lambda m}(\theta) & \phi_{|\lambda|+\downarrow}(r) \\ \beta_{\lambda m}(\theta) & \phi_{|\lambda|-\downarrow}(r)\end{pmatrix}, \tag{14}$$

where the functions $\alpha_{\lambda m}(\theta)$ and $\beta_{\lambda m}(\theta)$ are the polar-angle-dependent entries in eigenspinors of a massless Dirac fermion moving on a spherical shell [25,32]. Using the fact that they satisfy the set of relations

$$D\,\beta_{\lambda m}(\theta) = \lambda\,\alpha_{\lambda m}(\theta)\,,\quad D^\dagger\,\alpha_{\lambda m}(\theta) = \lambda\,\beta_{\lambda m}(\theta), \tag{15a}$$

$$\alpha_{\lambda m} = \left(\frac{\lambda}{|\lambda|}\right)^{\frac{1}{2}}\alpha_{|\lambda| m}\,,\quad \beta_{\lambda m} = \left(\frac{\lambda}{|\lambda|}\right)^{-\frac{1}{2}}\beta_{|\lambda| m}, \tag{15b}$$

we obtain the radial Schrödinger equation

$$[\mathcal{H}^{\perp}_{|\lambda|} + \mathcal{H}_V]\Phi_{|\lambda|}(r) = E_{|\lambda|}\,\Phi_{|\lambda|}(r) \qquad (16)$$

for the spinor $\Phi_{|\lambda|} = (\phi_{|\lambda|+\uparrow}, \phi_{|\lambda|-\uparrow}, \phi_{|\lambda|+\downarrow}, \phi_{|\lambda|-\downarrow})^T$, with the free radial Hamiltonian given by

$$\mathcal{H}^{\perp}_{|\lambda|} = \left\{\frac{\Delta_0}{2} + \frac{\gamma}{k_\Delta}\frac{1}{r^2}[|\lambda|^2 - \partial_r(r^2\,\partial_r)]\right\}\tau_z \otimes \sigma_0$$

$$- i\,\gamma\left(\partial_r + \frac{1}{r}\right)\tau_x \otimes \sigma_z$$

$$+ \frac{\gamma}{r}|\lambda|\left(\tau_x \otimes \sigma_x - \frac{1}{k_\Delta r}\tau_z \otimes \sigma_y\right). \qquad (17)$$

$$\Psi^{(n_{\mathrm{a}})}_{\lambda m}(\mathbf{r}) = \mathcal{U}(\theta,\varphi)\,\frac{e^{im\varphi}}{\sqrt{4\pi}}\left\{\begin{pmatrix}\alpha_{\lambda m}(\theta)\\0\\i\,\beta_{\lambda m}(\theta)\\0\end{pmatrix}\phi^{(n_{\mathrm{a}})}_{j+\uparrow}(r) + \begin{pmatrix}0\\\alpha_{\lambda m}(\theta)\\0\\-i\,\beta_{\lambda m}(\theta)\end{pmatrix}\phi^{(n_{\mathrm{a}})}_{j-\uparrow}(r)\right\}, \qquad (18a)$$

$$\Psi^{(n_{\mathrm{b}})}_{\lambda m}(\mathbf{r}) = \mathcal{U}(\theta,\varphi)\,\frac{e^{im\varphi}}{\sqrt{4\pi}}\left\{\begin{pmatrix}\alpha_{\lambda m}(\theta)\\0\\-i\,\beta_{\lambda m}(\theta)\\0\end{pmatrix}\phi^{(n_{\mathrm{b}})}_{j+\uparrow}(r) + \begin{pmatrix}0\\\alpha_{\lambda m}(\theta)\\0\\i\,\beta_{\lambda m}(\theta)\end{pmatrix}\phi^{(n_{\mathrm{b}})}_{j-\uparrow}(r)\right\}. \qquad (18b)$$

Here n_{a} and n_{b} are the radial-quantum-number labels for two sets of energy levels arising from two distinct secular equations. Adapting the approach presented in Ref. [32], it is possible to express the wave functions from Eqs. (18a) and (18b) in terms of spherical harmonics. This yields the results presented in Eqs. (2) above, where

$$\Psi^{(n)}_{\lambda m}(\mathbf{r}) \equiv \Psi^{(n)}_{jm+}(\mathbf{r}) \quad \text{for } n \in \{n_{\mathrm{a}}\} \text{ and } \lambda > 0$$
$$\text{or } n \in \{n_{\mathrm{b}}\} \text{ and } \lambda < 0, \qquad (19a)$$

$$\Psi^{(n)}_{\lambda m}(\mathbf{r}) \equiv \Psi^{(n)}_{jm-}(\mathbf{r}) \quad \text{for } n \in \{n_{\mathrm{a}}\} \text{ and } \lambda < 0$$
$$\text{or } n \in \{n_{\mathrm{b}}\} \text{ and } \lambda > 0, \qquad (19b)$$

and prefactors given by

$$C^{(n)}_{j\kappa} = \begin{cases} i^j & n \in \{n_{\mathrm{a}}\}, \kappa = + \text{ or } n \in \{n_{\mathrm{b}}\}, \kappa = -\\ -i^{j+1} & n \in \{n_{\mathrm{a}}\}, \kappa = - \text{ or } n \in \{n_{\mathrm{b}}\}, \kappa = +. \end{cases} \qquad (20)$$

Our route to obtain Eqs. (2) via the *Ansatz* Eq. (14) is inspired by a particular way of solving the Dirac equation on a spherical shell [25,30,32], but this method is far from unique. An equivalent radial Schrödinger equation and eigenstates having the same angular-coordinate dependencies as those in Eqs. (2) should transpire, e.g., from writing *Ansätze* for eigenstates of the original Hamiltonian Eq. (1) in terms of spinor spherical harmonics [53] and applying the mathematical identities satisfied by them [54].

B. Solution of the radial Schrödinger equation for a hard-wall mass confinement

Solution of the radial Schrödinger Eq. (16) for a hard-wall mass confinement defining a TI nanoparticle with radius R requires obtaining eigenstates of $\mathcal{H}^{\perp}_{j+\frac{1}{2}}$ given in Eq. (17) and forming linear combinations of these for fixed energy E that satisfy the hard-wall boundary condition at $r = R$. The secular

As previously discussed, e.g., in Ref. [32], $|\lambda|$ is related to the half-integer eigenvalue j of total angular momentum $\mathbf{J} \equiv (\mathbf{L} + \frac{\hbar}{2}\boldsymbol{\sigma})$ via $|\lambda| = j + \frac{1}{2}$ and therefore must be a nonzero integer. The quantum numbers $m = -j, -j+1, \ldots j$ are the eigenvalues of the angular-momentum projection and, thus, also assume half-integer values. With this additional insight, solution of the radial Schrödinger Eq. (16) can proceed for any specific potential $V(r)$. Because of the one-to-one correspondence between values of $|\lambda|$ and j, we can use both interchangeably as labels for radial spinor wave functions, $\Phi_{|\lambda|}(r) \equiv \Phi_j(r)$, and its components $\phi_{|\lambda|\tau\sigma}(r) \equiv \phi_{j\tau\sigma}(r)$. In the following Sec. II B, we consider the special case of a hard-wall confinement. Using results obtained there as input, the electronic eigenstates are found to be of the form

equation associated with the linear system of equations for the superposition coefficients yields the bound-state energies.

There is a set of propagating-wave-like eigenstates for $\mathcal{H}^{\perp}_{j+\frac{1}{2}}$ that have the general form

$$\Phi^{(\mathrm{D})}_{j,\mathrm{a}}(r) = \begin{pmatrix} j_{j-\frac{1}{2}}(k\,r)\\ i\,\gamma_k\,j_{j+\frac{1}{2}}(k\,r)\\ i\,j_{j-\frac{1}{2}}(k\,r)\\ \gamma_k\,j_{j+\frac{1}{2}}(k\,r)\end{pmatrix}, \qquad (21a)$$

$$\Phi^{(\mathrm{D})}_{j,\mathrm{b}}(r) = \begin{pmatrix} j_{j+\frac{1}{2}}(k\,r)\\ -i\,\gamma_k\,j_{j-\frac{1}{2}}(k\,r)\\ -i\,j_{j+\frac{1}{2}}(k\,r)\\ \gamma_k\,j_{j-\frac{1}{2}}(k\,r)\end{pmatrix}, \qquad (21b)$$

where $j_\nu(\cdot)$ are spherical Bessel functions of the first kind [55] (not to be confused with the quantum number j of total angular momentum), $k > 0$ is a real number, and normalization factors have been omitted because they get absorbed into the coefficients in the bound-state linear combination. The energy eigenvalues are given by

$$\tilde{E}^{(\mathrm{D})}_\pm(k) = \pm\sqrt{\tilde{k}^4 + (1 + \tilde{\Delta}_0)\tilde{k}^2 + \frac{\tilde{\Delta}_0^2}{4}}, \qquad (22)$$

and the parameter entering corresponding eigenspinors can be found from the general expression

$$\gamma_k = \mathrm{sgn}(E)\sqrt{\frac{2\tilde{E} - \tilde{\Delta}_0 - 2\tilde{k}^2}{2\tilde{E} + \tilde{\Delta}_0 + 2\tilde{k}^2}}. \qquad (23)$$

Here we started using natural units for energies and wave numbers via the definitions $\tilde{k} = k/k_\Delta$ and $\tilde{E} = E/(\gamma k_\Delta)$. The particular form of the eigenstates given in Eqs. (21) is

reminiscent of confined-Dirac-particle states [23,35,56]. The absence of spherical Bessel functions of the second kind from the wave-function *Ansatz* in Eqs. (21) is dictated by the necessity of wave functions to be well-behaved at $r = 0$.

There exists another set of eigenstates for $\mathcal{H}^\perp_{j+\frac{1}{2}}$ that are evanescent in character,

$$\Phi^{(B)}_{j,a}(r) = \frac{1}{\sqrt{q\,r}} \begin{pmatrix} \bar{\gamma}_q\, I_j(q\,r) \\ i\, I_{j+1}(q\,r) \\ i\, \bar{\gamma}_q\, I_j(q\,r) \\ I_{j+1}(q\,r) \end{pmatrix}, \qquad (24a)$$

$$\Phi^{(B)}_{j,b}(r) = \frac{1}{\sqrt{q\,r}} \begin{pmatrix} -\bar{\gamma}_q\, I_{j+1}(q\,r) \\ -i\, I_j(q\,r) \\ i\, \bar{\gamma}_q\, I_{j+1}(q\,r) \\ I_j(q\,r) \end{pmatrix}, \qquad (24b)$$

where the spinor entries are modified spherical Bessel functions of the first kind [55], and $q > 0$ is real. The associated energy eigenvalues are

$$\tilde{E}^{(B)}_\pm(q) = \pm\sqrt{\tilde{q}^4 - (1 + \tilde{\Delta}_0)\tilde{q}^2 + \frac{\tilde{\Delta}_0^2}{4}}, \qquad (25)$$

and

$$\bar{\gamma}_q = \sqrt{\frac{2\tilde{q}^2 - \tilde{\Delta}_0 - 2\tilde{E}}{2\tilde{q}^2 - \tilde{\Delta}_0 + 2\tilde{E}}}. \qquad (26)$$

The consideration of such evanescent free-particle eigenstates in the context of BHZ-type model Hamiltonians [18,57] is required for mathematical consistency, but their physical significance is limited [58–60].

Having determined the eigenstates of $\mathcal{H}^\perp_{j+\frac{1}{2}}$, we can make an *Ansatz* for the wave function of hard-wall-confined electrons in the TI nanoparticle in the form of superpositions

$$\Phi^{(n)}_j(r) = c^{(D)}_{n,j,a}\, \Phi^{(D)}_{j,a}(r) + c^{(B)}_{n,j,a}\, \Phi^{(B)}_{j,a}(r)$$
$$+ c^{(D)}_{n,j,b}\, \Phi^{(D)}_{j,b}(r) + c^{(B)}_{n,j,b}\, \Phi^{(B)}_{j,b}(r) \qquad (27)$$

of such eigenstates for fixed energy E and require that the boundary condition $\Phi^{(n)}_j(R) = 0$ is satisfied. The associated system of linear equations for the coefficients $c^{(D,B)}_{n,j,a/b}$ has nontrivial solutions only if one of the secular equations

$$\gamma_k\, \bar{\gamma}_q = \begin{cases} \dfrac{I_{j+1}(qR)}{I_j(qR)} \dfrac{j_{j-\frac{1}{2}}(kR)}{j_{j+\frac{1}{2}}(kR)} & \text{case a} \\[3mm] -\dfrac{I_j(qR)}{I_{j+1}(qR)} \dfrac{j_{j+\frac{1}{2}}(kR)}{j_{j-\frac{1}{2}}(kR)} & \text{case b,} \end{cases} \qquad (28)$$

is fulfilled. In Eq. (28), the quantities k, q, γ_k, and $\bar{\gamma}_q$ are functions of E, given explicitly by [61]

$$\tilde{k} = \left[\frac{1}{2}\left(\sqrt{(1 + \tilde{\Delta}_0)^2 + 4\tilde{E}^2 - \tilde{\Delta}_0^2} - 1 - \tilde{\Delta}_0\right)\right]^{\frac{1}{2}}, \quad (29a)$$

$$\tilde{q} = \left[\frac{1}{2}\left(\sqrt{(1 + \tilde{\Delta}_0)^2 + 4\tilde{E}^2 - \tilde{\Delta}_0^2} + 1 + \tilde{\Delta}_0\right)\right]^{\frac{1}{2}}, \quad (29b)$$

$$\gamma_k = \text{sgn}(\tilde{E}) \left[\frac{2\tilde{E} - \sqrt{(1 + \tilde{\Delta}_0)^2 + 4\tilde{E}^2 - \tilde{\Delta}_0^2} + 1}{2\tilde{E} + \sqrt{(1 + \tilde{\Delta}_0)^2 + 4\tilde{E}^2 - \tilde{\Delta}_0^2} - 1}\right]^{\frac{1}{2}}, \quad (29c)$$

$$\bar{\gamma}_q = \left[\frac{\sqrt{(1 + \tilde{\Delta}_0)^2 + 4\tilde{E}^2 - \tilde{\Delta}_0^2} + 1 - 2\tilde{E}}{\sqrt{(1 + \tilde{\Delta}_0)^2 + 4\tilde{E}^2 - \tilde{\Delta}_0^2} + 1 + 2\tilde{E}}\right]^{\frac{1}{2}}. \quad (29d)$$

Solution of Eq. (28) for cases a and b yields associated series of quantized energy values $E^{(n_a)}_j$ and $E^{(n_b)}_j$, respectively. By construction, these satisfy $|E^{(n_{a/b})}_j| \geqslant |\Delta_0|/2$. The coefficients in the superposition (27) of corresponding bound states are straightforwardly found to be

$$c^{(D)}_{n_a,j,a} = N_{n_a,j}\,, \ c^{(B)}_{n_a,j,a} = N_{n_a,j}\, \xi_{n_a,j,a}\,, \ c^{(D)}_{n_a,j,b} = c^{(B)}_{n_a,j,b} = 0, \tag{30a}$$

$$c^{(D)}_{n_b,j,b} = N_{n_b,j}\,, \ c^{(B)}_{n_b,j,b} = N_{n_b,j}\, \xi_{n_b,j,b}\,, \ c^{(D)}_{n_b,j,a} = c^{(B)}_{n_b,j,a} = 0, \tag{30b}$$

with normalisation factors $N_{n_{a/b},j}$ and the parameters

$$\xi_{n_a,j,a} = - \frac{\gamma_k\, \sqrt{qR}\, j_{j+\frac{1}{2}}(kR)}{I_{j+1}(qR)} \Bigg|_{E=E^{(n_a)}_j}, \qquad (30c)$$

$$\xi_{n_b,j,b} = - \frac{\gamma_k\, \sqrt{qR}\, j_{j-\frac{1}{2}}(kR)}{I_j(qR)} \Bigg|_{E=E^{(n_b)}_j}. \qquad (30d)$$

Motivated by the well-known [18,23,57,62] existence of evanescent states having $|E| < |\Delta_0|/2$ in the topological regime [63] where $\Delta_0 < 0$, we consider also the modified *Ansatz*

$$\Phi^{(n)}_j(r) = c^{(P)}_{n,j,a}\, \Phi^{(P)}_{j,a}(r) + c^{(B)}_{n,j,a}\, \Phi^{(B)}_{j,a}(r)$$
$$+ c^{(P)}_{n,j,b}\, \Phi^{(P)}_{j,b}(r) + c^{(B)}_{n,j,b}\, \Phi^{(B)}_{j,b}(r), \qquad (31)$$

which is obtained by replacing the propagating-wave-like part $c^{(D)}_{n,j,a/b}\, \Phi^{(D)}_{j,a/b}(r)$ in Eq. (27) by $c^{(P)}_{n,j,a/b}\, \Phi^{(P)}_{j,a/b}(r)$ with the evanescent-wave spinors [64]

$$\Phi^{(P)}_{j,a}(r) = \frac{1}{\sqrt{\bar{k}\,r}} \begin{pmatrix} I_j(\bar{k}\,r) \\ -i\, \bar{\gamma}_{\bar{k}}\, I_{j+1}(\bar{k}\,r) \\ i\, I_j(\bar{k}\,r) \\ -\bar{\gamma}_{\bar{k}}\, I_{j+1}(\bar{k}\,r) \end{pmatrix}, \qquad (32a)$$

$$\Phi^{(P)}_{j,b}(r) = \frac{1}{\sqrt{\bar{k}\,r}} \begin{pmatrix} i\, I_{j+1}(\bar{k}\,r) \\ \bar{\gamma}_{\bar{k}}\, I_j(\bar{k}\,r) \\ I_{j+1}(\bar{k}\,r) \\ i\, \bar{\gamma}_{\bar{k}}\, I_j(\bar{k}\,r) \end{pmatrix}. \qquad (32b)$$

The energy-dependent parameters entering Eqs. (32) are

$$\tilde{\bar{k}} = \left[\frac{1}{2}\left(1 + \tilde{\Delta}_0 - \sqrt{(1 + \tilde{\Delta}_0)^2 + 4\tilde{E}^2 - \tilde{\Delta}_0^2}\right)\right]^{\frac{1}{2}}, \quad (33a)$$

$$\bar{\gamma}_{\bar{k}} = \text{sgn}(\Delta_0) \left[\frac{\sqrt{(1 + \tilde{\Delta}_0)^2 + 4\tilde{E}^2 - \tilde{\Delta}_0^2} - 1 - 2\tilde{E}}{\sqrt{(1 + \tilde{\Delta}_0)^2 + 4\tilde{E}^2 - \tilde{\Delta}_0^2} - 1 + 2\tilde{E}}\right]^{\frac{1}{2}}. \tag{33b}$$

Imposing the hard-wall boundary condition at $r = R$ yields the secular equations

$$-\bar{\gamma}_{\bar{k}}\,\bar{\gamma}_q = \begin{cases} \dfrac{I_{j+1}(qR)}{I_j(qR)}\,\dfrac{I_j(\bar{k}R)}{I_{j+1}(\bar{k}R)} & \text{case a,} \\[3mm] \dfrac{I_j(qR)}{I_{j+1}(qR)}\,\dfrac{I_{j+1}(\bar{k}R)}{I_j(\bar{k}R)} & \text{case b.} \end{cases} \quad (34)$$

The coefficients in the *Ansatz* given in Eq. (31) and involving only evanescent eigenstates of $\mathcal{H}^{\perp}_{j+\frac{1}{2}}$ are

$$c^{(\mathrm{P})}_{n_{\mathrm{a}},j,\mathrm{a}} = \bar{N}_{n_{\mathrm{a}},j}\,, \quad c^{(\mathrm{B})}_{n_{\mathrm{a}},j,\mathrm{a}} = \bar{N}_{n_{\mathrm{a}},j}\,\bar{\xi}_{n_{\mathrm{a}},j,\mathrm{a}}\,,$$
$$c^{(\mathrm{P})}_{n_{\mathrm{a}},j,\mathrm{b}} = c^{(\mathrm{B})}_{n_{\mathrm{a}},j,\mathrm{b}} = 0\,, \quad (35a)$$

$$c^{(\mathrm{P})}_{n_{\mathrm{b}},j,\mathrm{b}} = \bar{N}_{n_{\mathrm{b}},j}\,, \quad c^{(\mathrm{B})}_{n_{\mathrm{b}},j,\mathrm{b}} = \bar{N}_{n_{\mathrm{b}},j}\,\bar{\xi}_{n_{\mathrm{b}},j,\mathrm{b}}\,,$$
$$c^{(\mathrm{P})}_{n_{\mathrm{b}},j,\mathrm{a}} = c^{(\mathrm{B})}_{n_{\mathrm{b}},j,\mathrm{a}} = 0\,, \quad (35b)$$

with the parameters

$$\bar{\xi}_{n_{\mathrm{a}},j,\mathrm{a}} = \bar{\gamma}_{\bar{k}}\sqrt{\frac{q}{\bar{k}}}\,\frac{I_{j+1}(\bar{k}R)}{I_{j+1}(qR)}\bigg|_{E=E^{(n_{\mathrm{a}})}_j}\,, \quad (35c)$$

$$\bar{\xi}_{n_{\mathrm{b}},j,\mathrm{b}} = -i\,\bar{\gamma}_{\bar{k}}\sqrt{\frac{q}{\bar{k}}}\,\frac{I_j(\bar{k}R)}{I_j(qR)}\bigg|_{E=E^{(n_{\mathrm{b}})}_j}\,. \quad (35d)$$

The general form Eq. (14) of TI-nanoparticle bound-state wave functions, together with the *Ansätze* in Eqs. (27) and (31) [using also Eqs. (21), (24), and (32)] implies that the electron eigenstates in TI nanoparticles can be written as given in Eqs. (18a) and (18b). These expressions form the basis for deriving Eqs. (2), which is one of the main results of this paper. We use the general convention where energy levels for fixed j have labels n such that $E^{(n')}_j > E^{(n)}_j$ for $n' > n$, and $n > 0$ ($n < 0$) if $E^{(n)}_j > 0$ ($E^{(n)}_j < 0$). In addition to the quantized energies among any fixed-j series that arise as solutions of the secular Eqs. (28), the other secular Eq. (34) yields two more bound-state levels with energies within the bulk-material band gap when Δ_0 is negative and j below an R-dependent critical value j_{c}. For large R, j_{c} is also large, and the many solutions of Eq. (34) correspond to the topologically protected surface states of a bulk-TI material. Reducing R successively eliminates such solutions for higher j. Eventually, at $R = R_{\mathrm{c}}$, the energies of the $j = 1/2$ subgap bound states are pushed beyond $\pm|\Delta_0|/2$ and the TI-nanoparticle spectrum becomes noninverted. Figure 1 illustrates this general behavior. Assuming $qR \gg 1$ (which is typically satisfied) and $\Delta_0/(\gamma k_\Delta) > -1/2$ (which can be violated in existing materials), we find the analytical expressions

$$j_{\mathrm{c}} = \left\lfloor \sqrt{1 + \frac{\Delta_0}{\gamma k_\Delta}\frac{R}{R_0}} - 1 \right\rfloor, \quad (36a)$$

$$R_{\mathrm{c}} = \frac{3}{2}\frac{R_0}{\sqrt{1 + \Delta_0/(\gamma k_\Delta)}}. \quad (36b)$$

III. OPTICAL TRANSITIONS BETWEEN BOUND STATES IN TI NANOPARTICLES

Optical spectroscopy provides a useful tool to study the electronic structure of semiconductor nanomaterials [65,66], including single nanoparticles [67] and their ensembles [68]. In the following, we explore how the special properties of TI nanoparticles are manifested in their optical spectra. We start by discussing the general theoretical approach for treating confined multiband systems and then focus on our particular system of interest.

Electron states in the TI nanoparticle have the form

$$\big|\Psi^{(n)}_{jm\kappa}(\mathbf{r})\big\rangle = \sum_{\tau\sigma}\big[\Psi^{(n)}_{jm\kappa}(\mathbf{r})\big]_{\tau\sigma}|\tau\,\sigma\rangle, \quad (37)$$

where the $|\tau\,\sigma\rangle$ are the band-edge basis functions [37–39] listed in Eq. (3), and $[\Psi^{(n)}_{jm\kappa}(\mathbf{r})]_{\tau\sigma}$ denote entries in the envelope-function spinor $\Psi^{(n)}_{jm\kappa}(\mathbf{r})$ given in Eqs. (2). Optical transitions of electrons in this system are mediated by the dipole matrix element, which is most generally given as the sum of two contributions [69],

$$\mathbf{d}^{n'j'm'\kappa'}_{njm\kappa} = \boldsymbol{\mathcal{D}}^{n'j'm'\kappa'}_{njm\kappa} + \boldsymbol{\mathcal{B}}^{n'j'm'\kappa'}_{njm\kappa}, \quad (38)$$

where

$$\boldsymbol{\mathcal{D}}^{n'j'm'\kappa'}_{njm\kappa} = \sum_{\tau\sigma}\int d^3r\,\big[\Psi^{(n')}_{j'm'\kappa'}(\mathbf{r})\big]^*_{\tau\sigma}\,e\,\mathbf{r}\,\big[\Psi^{(n)}_{jm\kappa}(\mathbf{r})\big]_{\tau\sigma} \quad (39)$$

is the dipole matrix element for the envelope part of the electronic wave functions (e is the electron charge), and

$$\boldsymbol{\mathcal{B}}^{n'j'm'\kappa'}_{njm\kappa} = \sum_{\substack{\tau\tau'\\\sigma\sigma'}}\mathcal{F}^{n'j'm'\kappa'\tau'\sigma'}_{njm\kappa\tau\sigma}\,\mathbf{d}^{\tau'\sigma'}_{\tau\sigma} \quad (40)$$

contains the contributions of dipole matrix elements $\mathbf{d}^{\tau'\sigma'}_{\tau\sigma} \equiv \langle\tau'\sigma'|e\,\mathbf{r}|\tau\sigma\rangle$ between band-edge basis states, which are renormalized by the form factors

$$\mathcal{F}^{n'j'm'\kappa'\tau'\sigma'}_{njm\kappa\tau\sigma} = \int d^3r\,\big[\Psi^{(n')}_{j'm'\kappa'}(\mathbf{r})\big]^*_{\tau'\sigma'}\,\big[\Psi^{(n)}_{jm\kappa}(\mathbf{r})\big]_{\tau\sigma}. \quad (41)$$

When optical properties of wide-band-gap semiconductor materials are discussed, the basis-function-related contributions $\boldsymbol{\mathcal{B}}^{n'j'm'\kappa'}_{njm\kappa}$ are understood to represent interband transitions [65] occurring between states from the valence and conduction bands. In contrast, the envelope-function contributions $\boldsymbol{\mathcal{D}}^{n'j'm'\kappa'}_{njm\kappa}$ in such systems are referred to as intraband or intersubband because they involve initial and final states that are size-quantized levels deriving from the same (either conduction or valence) band. In our present case of interest, these two types of contributions to the optical matrix element cannot be neatly classified as either interband or intraband anymore, as the amplitude of every possible transition will be influenced significantly by both [36].

The fundamental relationship [65] between optical matrix elements for band-edge basis functions and linear-in-$\mathbf{k}$ terms in the $\mathbf{k}\cdot\mathbf{p}$ Hamiltonian Eq. (1) implies

$$\mathbf{d}^{\tau'\sigma'}_{\tau\sigma} = \tau\,\frac{i\,e}{\Delta_0}\,(\nabla_{\mathbf{k}}H|_{\mathbf{k}=\mathbf{0}})^{\tau'\sigma'}_{\tau\sigma}, \quad (42)$$

where we use the notation $(O)^{\tau'\sigma'}_{\tau\sigma}$ to indicate matrix elements of an operator O acting in $\mathbf{k}\cdot\mathbf{p}$ space. Using Eq. (42), we can conveniently rewrite the basis-function contribution to the optical dipole matrix element as

$$\boldsymbol{\mathcal{B}}^{n'j'm'\kappa'}_{njm\kappa} \equiv \frac{e\,R_0}{2}\int d^3r\,\big[\Psi^{(n')}_{j'm'\kappa'}(\mathbf{r})\big]^\dagger\,\tau_y\otimes\boldsymbol{\sigma}\,\Psi^{(n)}_{jm\kappa}(\mathbf{r}). \quad (43)$$

Together with Eq. (39), we can thus express the total dipole matrix element for optical transitions entirely within

envelope-function space as shown in Eq. (5), with the operator **d** given in Eq. (4).

In the calculation of the envelope-function part Eq. (39) of the optical-dipole matrix element Eq. (38), we employ the standard [51] representation of real-space coordinates in terms of spherical harmonics,

$$x \pm i y = \mp \sqrt{\frac{8\pi}{3}} \, r \, Y_1^{\pm 1}(\theta, \varphi), \tag{44}$$

$$z = \sqrt{\frac{4\pi}{3}} \, r \, Y_1^0(\theta, \varphi). \tag{45}$$

We also apply a well-known integral identity for spherical harmonics [see, e.g., Eq. (3.8.73) from Ref. [46]] to obtain

$$\int_0^\pi d\theta \, \sin\theta \int_0^{2\pi} d\varphi \, \left[Y_{l'}^{m'}(\theta, \varphi) \right]^* Y_1^{m_1}(\theta, \varphi) \, Y_l^m(\theta, \varphi)$$
$$= \sqrt{\frac{3}{4\pi}} \sqrt{\frac{2l+1}{2l'+1}} \, \langle l \, 0 \,; 1 \, 0 \,|\, l' \, 0 \rangle \, \langle l \, m \,; 1 \, m_1 \,|\, l' \, m' \rangle, \tag{46}$$

where the symbol $\langle l_1 m_1 ; l_2 m_2 | l m \rangle$ is used to denote Clebsch-Gordon coefficients [46]. Algebraic simplification then yields the terms in Eqs. (6) that are proportional to $\mathcal{R}_{n\,j}^{n'j'}$. Similarly, the terms in Eqs. (6) that are proportional to the overlap integrals $\mathcal{S}_{n\,j,\tau}^{n'j',\tau'}$ are obtained from calculating the basis-function contribution Eq. (43) to the optical-dipole

matrix element Eq. (38) using the orthogonality relation for spherical harmonics.

Results from Sec. II imply that in-gap bound states from the case-a series have eigenenergies with equal magnitude but opposite sign as those of the case-b series. Each of these levels is degenerate in the parity-related quantum number κ. Hence, in an undoped TI nanoparticle, optical transitions can occur between the opposite-energy eigenstates, and the energy cutoff for photon absorption and emission via single-electron transitions is given by the TI-nanoparticle band gap $2 \cdot \min\{E_j^{(1)}\}$. We illustrate the allowed optical transitions between topological (i.e., in-gap) nanoparticle bound states in Fig. 3. Such single-particle transitions will dominantly determine the optical properties of nanoparticles with sizes smaller than the charge-carriers' Bohr radius [70]. The total magnitude of optical transition matrix elements associated with such transitions is given by

$$(T_\pm)_{n\,j\,\kappa}^{n'j'\kappa'} = \sum_{m=-j}^j \left| (d_x \pm i d_y)_{n\,j\,m\,\kappa}^{n'j'm'\kappa'} \right|^2 \equiv \frac{2e^2 R^2}{3} \mathcal{T}_{n\,j\,\kappa}^{n'j'\kappa'}, \tag{47a}$$

$$(T_z)_{n\,j\,\kappa}^{n'j'\kappa'} = \sum_{m=-j}^j \left| (d_z)_{n\,j\,m\,\kappa}^{n'j'm'\kappa'} \right|^2 \equiv \frac{e^2 R^2}{3} \mathcal{T}_{n\,j\,\kappa}^{n'j'\kappa'}, \tag{47b}$$

with a dimensionless measure of the squared magnitude of the optical dipole vector defined as

$$\mathcal{T}_{n\,j\,\kappa}^{n'j'\kappa'} = \delta_{\kappa',\kappa} \sum_{\xi=\pm 1} \frac{(2j+\xi)[2(j+1)+\xi]}{2(2j+1+\xi)} \left| \frac{\mathcal{R}_{n\,j}^{n'j'}}{R} - i\kappa\xi \, \frac{R_0}{2R} \, \mathcal{S}_{n\,j,-\kappa\xi}^{n'j',\kappa\xi} \right|^2 \delta_{j',j+\xi}$$

$$+ \delta_{\kappa',-\kappa} \frac{2j+1}{4j(j+1)} \left| \frac{\mathcal{R}_{n\,j}^{n'j'}}{R} + i\kappa \, \frac{R_0}{2R} \left(j \, \mathcal{S}_{n\,j,-\kappa}^{n'j',\kappa} + (j+1) \, \mathcal{S}_{n\,j,\kappa}^{n'j',-\kappa} \right) \right|^2 \delta_{j',j}. \tag{48}$$

The nanoparticle-size dependence of $\mathcal{T}_{n\,j\,\kappa}^{n'j'\kappa'}$ for the two lowest-energy transitions is plotted in Fig. 4. It exhibits a confinement-induced parity-symmetry breaking that gets most pronounced in the small-size limit where transition amplitudes are dominated by overlap integrals $\mathcal{S}_{n\,j,\pm}^{n'j',\mp}$ whose magnitude deviates from unity.

IV. CONCLUSIONS AND OUTLOOK

We have solved analytically the quantum-confinement problem of charge carriers in spherical nanoparticles made from TI materials, extending previous results [25,36]. The mathematical formalism employed in our study unifies related multiband descriptions of semiconductor nanocrystals [47,48] and confined Dirac fermions [32,35,36,56]. Compact transcendental secular equations are obtained for the energies of both ordinary (i.e., deriving from linear combinations of propagating bulk states) and topological (i.e., constituting confined intrinsic surface states) bound-state levels. See Eqs. (28) and (34), respectively. Explicit results for the size dependence of topological-bound-state subgap energies calculated using parameters applicable to real materials are shown in Fig. 1.

Significant deviations from previously derived [25,36] asymptotic expressions arise already for not-so-small values of R/R_0, where R and R_0 are the nanoparticle radius and the bulk-material Compton length, respectively.

A universal form of the envelope-wave-function spinors for TI-nanoparticle bound states in terms of spherical harmonics is presented in Eqs. (2). These states are labeled by the half-integer quantum numbers for total angular momentum (j) and its projection onto an arbitrary axis (m), as well as a two-valued quantum number $\kappa = \pm 1$. States with fixed j, m, and κ are also eigenstates of parity with eigenvalue $(-1)^{j-\frac{\kappa}{2}}$.

We considered optical transitions between single-electron bound states in a TI nanoparticle via the conventional [65] electric-dipole coupling. Our approach describes both envelope-function- and basis-state-mediated transitions via a compact optical-dipole operator in envelope-function space [see Eqs. (4) and (5)], and general analytical results are obtained for the transition matrix elements [Eqs. (6)]. In addition to the previously discussed [36] transitions between levels where $j' - j = \pm 1$, we also identify possible transitions where $j' - j = 0$. The latter were not identified in Ref. [36]. The possibility to conserve total angular momentum in an optical transition arises because there exist TI-nanoparticle
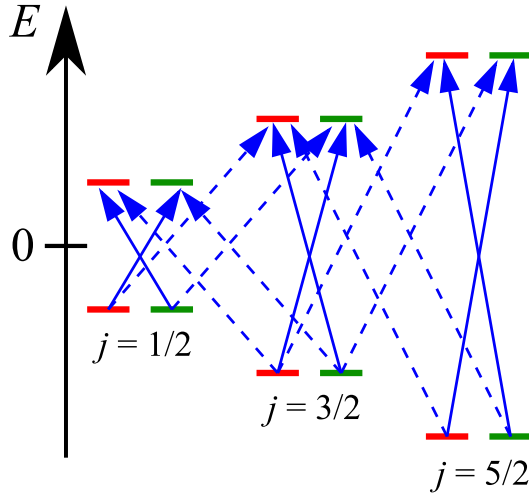
FIG. 3. Optical transitions in undoped TI nanoparticles between levels derived from topologically protected surface states. Red (green) color indicates states with parity-related quantum number $\kappa = +$ ($-$). Transitions conserving κ (illustrated by dashed-line arrows) require a change in the total-angular-momentum quantum number j by ± 1. Transitions conserving j (indicated by solid-line arrows) are possible between states having opposite κ. The selection rule $\Delta m = 0, \pm 1$ applies to all of these transitions.

bound states at any given j that have opposite parity. For such a pair of states [see their explicit expressions in Eqs. (2)], corresponding spinor entries have orbital angular momentum differing by one unit, as required for accommodating a photon's angular momentum. The multitude of possible transitions between topological bound-state levels in an undoped TI nanoparticle is illustrated in Fig. 3.

The effect of the nanoparticle size on optical transitions is contained in the radial-wave-function overlap integrals given in Eqs. (7) and (8). Their size dependence for the lowest subgap-energy bound state is plotted in Fig. 2. For $R \gg R_0$, the envelope-function contribution to the transition matrix element is $\propto R$, reflecting the surface-localized character of these states in this limit. However, significant deviations from this expected behavior occur already from $R \sim 10\,R_0$ for typical materials, and also the basis-state contribution starts to become relevant within this size range. The nanoparticle-radius dependence of transition-dipole magnitudes for the lowest-energy unconventional and conventional types of optical transitions is shown in Fig. 4. Both have similar order of magnitude and exhibit pronounced parity-symmetry breaking in the small-R limit.

Our results provide detailed information about how size quantization affects surface-state-related electronic and optical properties in TI nanoparticles, which has important practical implications. To start, the existence of additional optical transitions beyond those identified earlier in Ref. [36] requires re-evaluation of suggested schemes [36] to employ TI-nanoparticle states in quantum information processing. More generally, our theoretical description can serve as a starting point for developing any type of application that relies on specifics of the electronic energy spectrum and quantum transitions between TI-nanoparticle bound states.
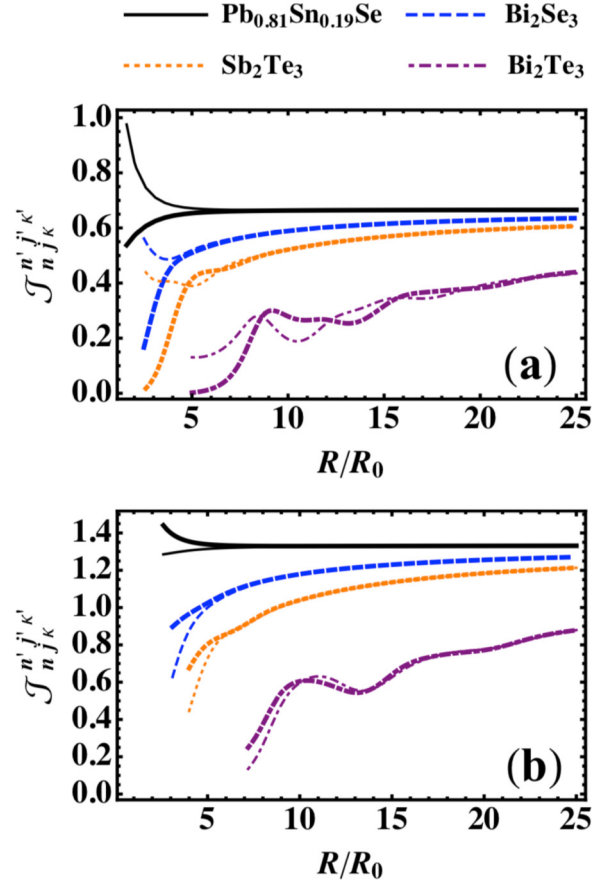

FIG. 4. The modulus squared of the dipole moment for optical transitions in a spherical topological-insulator nanoparticle with radius R is given by $e^2 R^2\, \mathcal{T}_{njk}^{n'j'\kappa'}$. Panel (a) plots the nanoparticle-size dependence of the dimensionless dipole magnitude $\mathcal{T}_{njk}^{n'j'\kappa'}$ for the lowest-energy transitions in an undoped nanoparticle, i.e., for $n = -1$, $n' = 1$, $j = j' = 1/2$, and $\kappa = -\kappa' = +/-$ (thick/thin curves). Panel (b) shows $\mathcal{T}_{njk}^{n'j'\kappa'}$ for the next-highest-energy transitions where $n = -1$, $n' = 1$, $j = j' - 1 = 1/2$, and $\kappa = \kappa' = +/-$ (thick/thin curves). Here $R_0 = 2\gamma/|\Delta_0|$ is the bulk Compton length, and the black solid (blue dashed, orange dotted, purple dot-dashed) curve is obtained for $\Delta_0/(\gamma k_\Delta) = -0.039$ (-1.2, -2.3, -9.5,), which is representative of $Pb_{0.81}Sn_{0.19}Se$ (Bi_2Se_3, Sb_2Te_3, Bi_2Te_3).

For example, some of the currently envisioned uses of TI nanoparticles in optoelectronic [9,14] and thermoelectric [17] devices are contingent on the presence of topologically protected surface states. Recognizing the existence, and strongly materials-dependent magnitude, of a critical radius below which the topological surface states disappear is therefore of crucial importance. The emergent gaplessness of the Bi_2Te_3-nanopoarticle spectrum for certain sizes [see Fig. 1(b)] could become a platform for intriguing applications, including the possibility to host unconventional Majorana excitations as was proposed for gapless TI nanoribbons [71].

Our theoretical approach is based on the envelope-function continuum-model description for the TI band structure [37–39]. The mathematical structure of this formalism necessitates inclusion of fast-decaying wave-function contributions [those given in Eqs. (24)] representing the effect of

remote bands whose influence on observable physical quantities needs to be interpreted with caution [58–60]. Typically, the physically significant wave functions from Eqs. (21) and (32) dominate the system's low-energy properties. However, in confined TI materials with large values of $|\Delta_0|/(\gamma k_\Delta)$, we find that both types of evanescent states [(32) and (24)] present in the subgap bound-state wave functions Eq. (31) can be relevant on comparable length scales, signaling the impending breakdown of the continuum-model approach. Nevertheless, qualitative trends exhibited in size-dependent physical properties are expected to be accurate even relatively close to this extreme limit. Thus, our approach serves as a useful tool for modeling the effect of quantum confinement in TI nanoparticles, especially as long as atomistic band-structure calculations [72] can be performed only for very small systems [5,41]. Results presented here also provide an interesting reference point for understanding size-quantization effects in other TI nanostructures such as cylindrical quantum dots [73] or nanowires with finite [74] and infinite length [75–77].

In future work, the obtained single-particle wave functions for TI-nanoparticle bound states could serve as input to discuss many-body effects due to Coulomb interactions. In particular, exploring the properties of excitons would be of interest in the context of optical properties of TI nanoparticles [24]. The multiband spinor structure of charge carriers' quantum states should result in a form-factor renormalization of the Coulomb-potential matrix element similar to previously considered situations [78]. Interesting properties associated with two-particle states of Dirac-like carriers [79,80], e.g., the recently predicted existence of an internal angular momentum of the exciton [81], could be elucidated in greater detail. Early numerical studies [24] can serve as a benchmark for evaluating the accuracy of approximate analytical results.

ACKNOWLEDGMENTS

[1] A. D. Yoffe, Low-dimensional systems: Quantum size effects and electronic properties of semiconductor microcrystallites (zero-dimensional systems) and some quasi-two-dimensional systems, Adv. Phys. **42**, 173 (1993).

[2] A. L. Efros and M. Rosen, The electronic structure of semiconductor nanocrystals, Annu. Rev. Mater. Sci. **30**, 475 (2000).

[3] S. Cho, D. Kim, P. Syers, N. P. Butch, J. Paglione, and M. S. Fuhrer, Topological insulator quantum dot with tunable barriers, Nano Lett. **12**, 469 (2012).

[4] S. V. Kershaw, A. S. Susha, and A. L. Rogach, Narrow bandgap colloidal metal chalcogenide quantum dots: Synthetic methods, heterostructures, assemblies, electronic and infrared optical properties, Chem. Soc. Rev. **42**, 3033 (2013).

[5] A. Vargas, S. Basak, F. Liu, B. Wang, E. Panaitescu, H. Lin, R. Markiewicz, A. Bansil, and S. Kar, The changing colors of a quantum-confined topological insulator, ACS Nano **8**, 1222 (2014).

[6] G. Z. Jia, W. K. Lou, F. Cheng, X. L. Wang, J. H. Yao, N. Dai, H. Q. Lin, and K. Chang, Excellent photothermal conversion of core/shell CdSe/Bi$_2$Se$_3$ quantum dots, Nano Res. **8**, 1443 (2015).

[7] A. Vargas, F. Liu, and S. Kar, Giant enhancement of light emission from nanoscale Bi$_2$Se$_3$, Appl. Phys. Lett. **106**, 243107 (2015).

[8] M. S. Claro, I. Levy, A. Gangopadhyay, D. J. Smith, and M. C. Tamargo, Self-assembled bismuth selenide (Bi$_2$Se$_3$) quantum dots grown by molecular beam epitaxy, Sci. Rep. **9**, 3370 (2019).

[9] M. S.Rider, M. Sokolikova, S. M. Hanham, M. Navarro-Cía, P. Haynes, D. Lee, M. Daniele, M. C. Guidi, C. Mattevi, S. Lupi, and V. Giannini, Experimental signature of a topological quantum dot, arXiv:1905.06193.

[10] S. S. Hong, D. Kong, and Y. Cui, Topological insulator nanostructures, MRS Bull. **39**, 873 (2014).

[11] M. Z. Hasan and C. L. Kane, *Colloquium*: Topological insulators, Rev. Mod. Phys. **82**, 3045 (2010).

[12] M. Z. Hasan and J. E. Moore, Three-dimensional topological insulators, Annu. Rev. Condens. Matter Phys. **2**, 55 (2011).

[13] M. Z. Hasan, S.-Y. Xu, and G. Bian, Topological insulators, topological superconductors and Weyl fermion semimetals: Discoveries, perspectives and outlooks, Phys. Scr. **2015**, 014001 (2015).

[14] A. Politano, L. Viti, and M. S. Vitiello, Optoelectronic devices, plasmonics, and photonics with topological insulators, APL Mater. **5**, 035504 (2017).

[15] J. W. McIver, D. Hsieh, H. Steinberg, P. Jarillo-Herrero, and N. Gedik, Control over topological insulator photocurrents with light polarization, Nat. Nanotech. **7**, 96 (2012).

[16] J. Tian, S. Hong, I. Miotkowski, S. Datta, and Y. P. Chen, Observation of current-induced, long-lived persistent spin polarization in a topological insulator: A rechargeable spin battery, Sci. Adv. **3**, e1602531 (2017).

[17] N. Xu, Y. Xu, and J. Zhu, Topological insulators for thermoelectrics, npj Quantum Mater. **2**, 51 (2017).

[18] B. Zhou, H.-Z. Lu, R.-L. Chu, S.-Q. Shen, and Q. Niu, Finite Size Effects on Helical Edge States in a Quantum Spin-Hall System, Phys. Rev. Lett. **101**, 246807 (2008).

[19] J. Linder, T. Yokoyama, and A. Sudbø, Anomalous finite size effects on surface states in the topological insulator Bi$_2$Se$_3$, Phys. Rev. B **80**, 205401 (2009).

[20] C.-X. Liu, H. J. Zhang, B. Yan, X.-L. Qi, T. Frauenheim, X. Dai, Z. Fang, and S.-C. Zhang, Oscillatory crossover from two-dimensional to three-dimensional topological insulators, Phys. Rev. B **81**, 041307(R) (2010).

[21] H.-Z. Lu, W.-Y. Shan, W. Yao, Q. Niu, and S.-Q. Shen, Massive Dirac fermions and spin physics in an ultrathin film of topological insulator, Phys. Rev. B **81**, 115407 (2010).

[22] M. Kotulla and U. Zülicke, Manipulating topological-insulator properties using quantum confinement, New J. Phys. **19**, 073025 (2017).

[23] L. Gioia, U. Zülicke, M. Governale, and R. Winkler, Dirac electrons in quantum rings, Phys. Rev. B **97**, 205421 (2018).

[24] N. Malkova and G. W. Bryant, Negative-band-gap quantum dots: Gap collapse, intrinsic surface states, excitonic response, and excitonic insulator phase, Phys. Rev. B **82**, 155314 (2010).

[25] K.-I. Imura, Y. Yoshimura, Y. Takane, and T. Fukui, Spherical topological insulator, Phys. Rev. B **86**, 235119 (2012).

[26] Y. Takane and K.-I. Imura, Unified description of Dirac electrons on a curved surface of topological insulators, J. Phys. Soc. Jpn. **82**, 074712 (2013).

[27] G. Siroki, D. K. K. Lee, P. D. Haynes, and V. Giannini, Single-electron induced surface plasmons on a topological nanoparticle, Nat. Commun. **7**, 12375 (2016).

[28] G. Siroki, P. D. Haynes, D. K. K. Lee, and V. Giannini, Protection of surface states in topological nanoparticles, Phys. Rev. Mater. **1**, 024201 (2017).

[29] H.-G. Zirnstein and B. Rosenow, Time-reversal-symmetric topological magnetoelectric effect in three-dimensional topological insulators, Phys. Rev. B **96**, 201112(R) (2017).

[30] T. Neupert, S. Rachel, R. Thomale, and M. Greiter, Interacting Surface States of Three-Dimensional Topological Insulators, Phys. Rev. Lett. **115**, 017001 (2015).

[31] A. C. Durst, Disorder-induced density of states on the surface of a spherical topological insulator, Phys. Rev. B **93**, 245424 (2016).

[32] A. A. Abrikosov, Fermion states on the sphere S^2, Int. J. Mod. Phys. A **17**, 885 (2002), see arXiv:hep-th/0212134 for an extended version that also contains a useful collection of relevant references.

[33] D.-H. Lee, Surface States of Topological Insulators: The Dirac Fermion in Curved Two-Dimensional Spaces, Phys. Rev. Lett. **103**, 196804 (2009).

[34] V. Parente, P. Lucignano, P. Vitale, A. Tagliacozzo, and F. Guinea, Spin connection and boundary states in a topological insulator, Phys. Rev. B **83**, 075424 (2011).

[35] R. Layeghnejad, M. Zare, and R. Moazzemi, Dirac particle in a spherical scalar potential well, Phys. Rev. D **84**, 125026 (2011).

[36] H. P. Paudel and M. N. Leuenberger, Three-dimensional topological insulator quantum dot for optically controlled quantum memory and quantum computing, Phys. Rev. B **88**, 085316 (2013).

[37] H. Zhang, C.-X. Liu, X.-L. Qi, X. Dai, Z. Fang, and S.-C. Zhang, Topological insulators in Bi_2Se_3, Bi_2Te_3, and Sb_2Te_3 with a single Dirac cone on the surface, Nat. Phys. **5**, 438 (2009).

[38] C.-X. Liu, X.-L. Qi, H. J. Zhang, X. Dai, Z. Fang, and S.-C. Zhang, Model Hamiltonian for topological insulators, Phys. Rev. B **82**, 045122 (2010).

[39] M. R. Brems, J. Paaske, A. M. Lunde, and M. Willatzen, Symmetry analysis of strain, electric and magnetic fields in the Bi_2Se_3-class of topological insulators, New J. Phys. **20**, 053041 (2018).

[40] The τ_j (σ_j) for $j = x, y, z$ are standard Pauli matrices for the pseudospin-1/2 (real-spin-1/2) degree of freedom, and τ_0 (σ_0)

is the identity operator in that subspace. The symbol $\otimes$ indicates the direct product of operators from pseudospin and real-spin spaces. The combinations $\sigma_\pm \equiv (\sigma_x \pm i\sigma_y)/2$ are ladder operators for real spin, and $\boldsymbol{\sigma}$ denotes the vector $(\sigma_x, \sigma_y, \sigma_z)$.

[41] I. A. Nechaev and E. E. Krasovskii, Relativistic $\mathbf{k} \cdot \mathbf{p}$ Hamiltonians for centrosymmetric topological insulators from *ab initio* wave functions, Phys. Rev. B **94**, 201410(R) (2016).

[42] E. G. Novik, A. Pfeuffer-Jeschke, T. Jungwirth, V. Latussek, C. R. Becker, G. Landwehr, H. Buhmann, and L. W. Molenkamp, Band structure of semimagnetic $Hg_{1-y}Mn_yTe$ quantum wells, Phys. Rev. B **72**, 035321 (2005).

[43] P. C. Klipstein, Structure of the quantum spin Hall states in HgTe/CdTe and InAs/GaSb/AlSb quantum wells, Phys. Rev. B **91**, 035310 (2015).

[44] B. A. Assaf, T. Phuphachong, V. V. Volobuev, G. Bauer, G. Springholz, L.-A. de Vaulchier, and Y. Guldner, Magnetooptical determination of a topological index, npj Quant. Mater. **2**, 26 (2017).

[45] B. A. Assaf, T. Phuphachong, V. V. Volobuev, A. Inhofer, G. Bauer, G. Springholz, L. A. de Vaulchier, and Y. Guldner, Massive and massless Dirac fermions in $Pb_{1-x}Sn_x$ Te topological crystalline insulator probed by magneto-optical absorption, Sci. Rep. **6**, 20323 (2016).

[46] J. J. Sakurai and J. Napolitano, *Modern Quantum Mechanics*, 2nd ed. (Addison-Wesley, San Francisco, 2011).

[47] V. I. Sheka and D. I. Sheka, Local states in a semiconductor with a narrow forbidden band, Zh. Eksp. Teor. Fiz. **51**, 1445 (1966) [Sov. Phys. JETP **24**, 975 (1967)].

[48] A. L. Efros and M. Rosen, Quantum size level structure of narrow-gap semiconductor nanocrystals: Effect of band coupling, Phys. Rev. B **58**, 7120 (1998).

[49] B. Thaller, *The Dirac Equation* (Springer, Berlin, 1992).

[50] Within a conventional nomenclature [65], the term proportional to the position vector $\mathbf{r}$ (the TI-material Compton length R_0) in Eq. (4) is associated with intraband (interband) transitions. This jargon is somewhat misleading in the case of narrow-gap (e.g., TI) materials [36]. More precisely, the first (second) term on the right-hand side of Eq. (4) pertains to dipole transitions mediated by the envelope part (the Bloch-function basis) of the confined-electron states.

[51] W. Greiner, *Quantum Mechanics Special Chapters* (Springer, Berlin, 1998).

[52] The degree of freedom associated with the quantum number σ is the projection of a real spin-1/2 angular momentum, but this is not the actual electron spin [39].

[53] D. A. Varshalovich, A. N. Moskalev, and V. K. Khersonskii, *Quantum Theory of Angular Momentum* (World Scientific, Singapore, 1988), Sec. 7.2 .

[54] R. Szmytkowski, Recurrence and differential relations for spherical spinors, J. Math. Chem. **42**, 397 (2007).

[55] M. Abramowitz and I. A. Stegun, *Handbook of Mathematical Functions* (Dover, New York, 1964).

[56] P. Alberto, C. Fiolhais, and V. M. S. Gil, Relativistic particle in a box, Eur. J. Phys. **17**, 19 (1996).

[57] B. A. Bernevig, T. L. Hughes, and S. Zhang, Quantum spin Hall effect and topological phase transition in HgTe quantum wells, Science **314**, 1757 (2006).

[58] S. R. White and L. J. Sham, Electronic Properties of Flat-Band Semiconductor Heterostructures, Phys. Rev. Lett. **47**, 879 (1981).

[59] M. F. H. Schuurmans and G. W. 't Hooft, Simple calculations of confinement states in a quantum well, Phys. Rev. B **31**, 8041 (1985).

[60] P. C. Klipstein, A $\mathbf{k} \cdot \mathbf{p}$ treatment of edge states in narrow 2D topological insulators, with standard boundary conditions for the wave function and its derivative, J. Phys.: Condens. Matter **30**, 275302 (2018).

[61] We find the expressions for $\tilde{k}$ and $\tilde{q}$ by solving for these in the relations $\tilde{E}_{\pm}^{(D)}(k) = \tilde{E}$ and $\tilde{E}_{\pm}^{(B)}(q) = \tilde{E}$, respectively. Then γ_k and $\bar{\gamma}_q$ are obtained by inserting the expressions found for $\tilde{k}$ and $\tilde{q}$ into Eqs. (23) and (26), respectively.

[62] B. A. Volkov and O. A. Pankratov, Two-dimensional massless electrons in an inverted contact, Pis'ma Zh. Eksp. Teor. Fiz. **42**, 145 (1985) [JETP Lett. **42**, 178 (1985)].

[63] A different type of intrinsic semiconductor-nanoparticle subgap state discussed in Ref. [82] has its origin in a sign change of effective masses [83] instead of a band inversion.

[64] Using identity 10.2.2 from Ref. [55], it can be shown that the spinors in Eqs. (32) are obtained from those in Eqs. (21) by making the replacements $k = i\tilde{k}$ and $\gamma_k = i\bar{\gamma}_{\tilde{k}}$.

[65] H. Haug and S. W. Koch, *Quantum Theory of the Optical and Electronic Properties of Semiconductors*, 4th ed. (World Scientific, Singapore, 2004).

[66] I. Pelant and J. Valenta, *Luminescence Spectroscopy of Semiconductors* (Oxford University Press, Oxford, UK, 2012).

[67] A. Gustafsson, M.-E. Pistol, L. Montelius, and L. Samuelson, Local probe techniques for luminescence studies of low-dimensional semiconductor structures, J. Appl. Phys. **84**, 1715 (1998).

[68] V. M. Fomin, V. N. Gladilin, J. T. Devreese, E. P. Pokatilov, S. N. Balaban, and S. N. Klimin, Photoluminescence of spherical quantum dots, Phys. Rev. B **57**, 2415 (1998).

[69] In our notation, initial (final) states are labeled by quantum numbers n, j, m, κ (n', j', m', κ'). Equation (38) is a generalization of Eq. (5.34) from Ref. [65] and, as the latter, relies on the assumption that the envelope-function part of electronic wave functions varies on much larger length scales than the basis functions.

[70] A. L. Efros and A. L. Efros, Interband absorption of light in a semiconductor sphere, Fiz. Tekh. Poluprovodn. **16**, 1209 (1982) [Sov. Phys. Semicond. **16**, 772 (1982)].

[71] J. Manousakis, A. Altland, D. Bagrets, R. Egger, and Y. Ando, Majorana qubits in a topological insulator nanoribbon architecture, Phys. Rev. B **95**, 165424 (2017).

[72] A. Bansil, H. Lin, and T. Das, *Colloquium*: Topological band theory, Rev. Mod. Phys. **88**, 021004 (2016).

[73] T. M. Herath, P. Hewageegana, and V. Apalkov, A quantum dot in topological insulator nanofilm, J. Phys.: Condens. Matter **26**, 115302 (2014).

[74] A. Kundu, A. Zazunov, A. L. Yeyati, T. Martin, and R. Egger, Energy spectrum and broken spin-surface locking in topological insulator quantum dots, Phys. Rev. B **83**, 125429 (2011).

[75] K.-I. Imura, Y. Takane, and A. Tanaka, Spin Berry phase in anisotropic topological insulators, Phys. Rev. B **84**, 195406 (2011).

[76] P. Iorio, C. A. Perroni, and V. Cataudella, Quantum interference effects in Bi_2Se_3 topological insulator nanowires with variable cross-section lengths, Eur. Phys. J. B **89**, 97 (2016).

[77] N. Virk, G. Autès, and O. V. Yazyev, Electronic properties of one-dimensional nanostructures of the Bi_2Se_3 topological insulator, Phys. Rev. B **97**, 165411 (2018).

[78] T. Kernreiter, M. Governale, R. Winkler, and U. Zülicke, Suppression of Coulomb exchange energy in quasi-two-dimensional hole systems, Phys. Rev. B **88**, 125309 (2013).

[79] J. Sabio, F. Sols, and F. Guinea, Two-body problem in graphene, Phys. Rev. B **81**, 045428 (2010).

[80] O. L. Berman, R. Y. Kezerashvili, and K. Ziegler, Coupling of two Dirac particles, Phys. Rev. A **87**, 042513 (2013).

[81] M. Trushin, M. O. Goerbig, and W. Belzig, Model Prediction of Self-Rotating Excitons in Two-Dimensional Transition-Metal Dichalcogenides, Phys. Rev. Lett. **120**, 187401 (2018).

[82] P. C. Sercel, A. L. Efros, and M. Rosen, Intrinsic Gap States in Semiconductor Nanocrystals, Phys. Rev. Lett. **83**, 2394 (1999).

[83] Y. R. Lin-Liu and L. J. Sham, Interface states and subbands in HgTe-CdTe heterostructures, Phys. Rev. B **32**, 5561 (1985).